

A surface strategy boosting the ethylene selectivity for CO₂ reduction and in situ mechanistic insights

Received: 14 April 2023

Accepted: 1 February 2024

Published online: 10 February 2024

Check for updates

Yinchao Yao^{1,6}, Tong Shi^{2,3,6}, Wenxing Chen¹, Jiehua Wu⁴, Yunying Fan⁵,
Yichun Liu⁵, Liang Cao²✉ & Zhuo Chen¹✉

Electrochemical reduction of carbon dioxide into ethylene, as opposed to traditional industrial methods, represents a more environmentally friendly and promising technical approach. However, achieving high activity of ethylene remains a huge challenge due to the numerous possible reaction pathways. Here, we construct a hierarchical nanoelectrode composed of CuO treated with dodecanethiol to achieve elevated ethylene activity with a Faradaic efficiency reaching 79.5%. Through on in situ investigations, it is observed that dodecanethiol modification not only facilitates CO₂ transfer and enhances *CO coverage on the catalyst surfaces, but also stabilizes Cu(100) facet. Density functional theory calculations of activation energy barriers of the asymmetrical C–C coupling between *CO and *CHO further support that the greatly increased selectivity of ethylene is attributed to the thiol-stabilized Cu(100). Our findings not only provide an effective strategy to design and construct Cu-based catalysts for highly selective CO₂ to ethylene, but also offer deep insights into the mechanism of CO₂ to ethylene.

The electrocatalytic conversion of carbon dioxide into high-value-added chemicals and fuels stands as a promising technological avenue for transforming waste into valuable resources and fostering the development of a sustainable, carbon-neutral society¹. Among various carbon dioxide reduction products, C₂₊ products are attracting attention due to their higher value, especially for ethylene as an essential building block in the chemical industry, emerging as a focal point in this realm^{2–7}. However, the efficient conversion of CO₂ to ethylene remains a formidable challenge. Notably, copper-based catalysts within the realm of transition metal catalysts have attracted considerable interest due to their excellent C₂₊ product selectivity^{3,5,6,8}. In general, the electrocatalytic CO₂ reduction reaction (CO₂RR) over copper-based catalysts involves three pivotal steps: efficient CO₂

diffusion into the catalyst interface, activation of CO₂ molecules at the interface, and concerted proton–electron transfer (CPET) steps, culminating in the formation of *CO intermediates^{9,10}. Lastly, catalysts must exhibit high activity in promoting the C–C coupling reaction to facilitate the production of C₂₊ products.

With considerable attention devoted to overcoming the limitations of the two formers, some effective strategies have been developed, such as developing efficient electrocatalysts¹¹, tailoring electrode–electrolyte interface¹², and optimizing the electrolyser design⁴. However, the C–C coupling is the most critical step in determining the selectivity and yield of various C₂₊ products^{13–15}. Moreover, there persists a lack of comprehensive consensus on the C–C coupling mechanism^{10,14}. Numerous approaches have been reported to promote

¹Energy & Catalysis Center, Department of Materials Physics and Chemistry, School of Materials Science and Engineering, Beijing Institute of Technology, 100081 Beijing, PR China. ²Institute of Catalysis, Department of Chemistry, Zhejiang University, Hangzhou 310058 Zhejiang, PR China. ³Inner Mongolia Key Laboratory of Chemistry and Physics of Rare Earth Materials, Department of Chemistry and Chemical Engineering, Inner Mongolia University, Hohhot 010021, PR China. ⁴SINOPEC (Beijing) Research Institute of Chemical Industry Co., Ltd, 100013 Beijing, PR China. ⁵School of Materials Science and Engineering, Kunming University of Science and Technology, Kunming 650093, PR China. ⁶These authors contributed equally: Yinchao Yao, Tong Shi.

✉ e-mail: liangcao@zju.edu.cn; zchen@bit.edu.cn

the C–C coupling on copper surfaces, including morphology tuning^{9,16}, crystal facet regulation^{17,18}, chemical state manipulation^{7,19,20}, and surface modification^{3,21}, with crystal facet being identified as a crucial parameter. According to the crystal structure of copper, Cu(100) with lower surface coordination numbers exhibits higher CO dimerization reactivity and C₂₊ product selectivity^{18,22,23}. Theoretical calculations indicate thermodynamic favorability for C–C coupling of the two *CO intermediates on Cu(100) to produce ethylene^{15,24,25}. Thus, controlled exposure of Cu(100) is deemed essential for facilitating ethylene selectivity. Experimental studies confirm that Cu cubes with rich (100) facets significantly increase the ethylene Faraday efficiency to 57%²⁶. However, dynamic reconstruction of the copper crystal face during CO₂RR, driven by its low cohesion energy, poses challenges in maintaining the crystal structure, exacerbated by CO₂RR intermediates^{22,27}. Therefore, to further enhance the selectivity of ethylene, it is imperative to improve the Cu(100) content of the catalyst while ensuring the stability of the Cu(100) crystalline surface during the CO₂RR reaction.

Herein, we employ a DDT-functionalized CuO hierarchical nanostructural electrode to achieve high selectivity of CO₂RR toward ethylene. The Faradaic efficiency (FE) of C₂H₄ product reaches up to 72%, marking an enhancement of more than 4-fold compared to the electrode without DDT treatment. In situ Raman and attenuated total reflectance-Fourier transform infrared (ATR-FTIR) spectroscopy results indicate that DDT facilitates CO₂ transport and enhances CO coverage on the catalyst surface. Moreover, in situ XRD and X-ray absorption spectroscopies (XAS) investigations elucidate that DDT stabilizes Cu(100) facets, thus promoting the C–C coupling. DFT²⁸ calculations further reveal that thiol stabilized Cu(100) facet can reduce the activation energy barrier of C–C coupling between *CO and *CHO, in which the intermediates are confirmed by in situ ATR-FTIR. This work paves a promising route for highly selective CO₂RR to ethylene through surface-modified Cu-based catalysts and deepens insights into the mechanism of CO₂RR to ethylene.

Results and discussion

Catalyst design and preparation

The electrocatalytic CO₂RR occurring at the interface between the electrode and electrolyte encompasses multiple stages: the diffusion of CO₂ onto the electrode surface, subsequent adsorption at the reaction site, concurrent transfer of electrons and protons, reduction to hydrocarbons, and eventual desorption. To address the simultaneous requirements of this aspects, we engineered a hierarchical nanostructural electrode with a hydrophobic surface as shown in Fig. 1a. Specifically, CuO nanowire arrays were prepared on a copper foam substrate through annealing the electrodeposited Cu(OH)₂ nanowire arrays, leading to a hierarchical nanostructure, and thus not only facilitating charge transfer via the ordered 1D channel but also exposing more active sites through the high surface area. Scanning electron microscopy (SEM) and transmission electron microscopy (TEM) confirmed the orderly arranged nanowire morphology of CuO (Supplementary Fig. 1). High-resolution TEM (HRTEM) and X-ray diffraction pattern showed that the crystal structure of nanowires was composed of Cu₂O and CuO (Supplementary Figs. 1 and 2). To build a hydrophobic interface while concurrently stabilizing the Cu(100) surface, we conducted a screening of potential molecules via DFT calculations combined with literature research. Based on DFT calculations of the adsorption energies of various alcohols, thiols, and amines with alkyl chains (inset in Fig. 1a), we selected the thiol molecule with the highest binding ability to the Cu(100) facets for surface modification. Additionally, the calculations indicated a stronger binding of the thiol molecule to Cu(100) than Cu(111), suggesting a preference for stabilizing the Cu(100) surface, as shown in Fig. 1a, Supplementary Fig. 3 and Supplementary Table 1, meaning that the thiol molecule can preferentially stabilize the Cu(100) surface. Consequently, a hydrophobic thiol salt layer was introduced on the CuO surface by immersing the

CuO nanoarrays into liquid DDT, creating a three-phase interface and thereby enhancing local CO₂ concentration. For convenience, the electrodes before and after DDT modification are denoted by CuO and CuO-SH, respectively. The contact angle test results show that a superhydrophobic interface was formed on the CuO-SH electrode's surface (Fig. 1b). Expectedly, the hierarchical nanostructure of CuO-SH was confirmed by SEM and TEM (Fig. 1b, c). Energy-dispersive X-ray spectroscopy (EDS) analyses in a STEM showed a uniform distribution of S and C environments on the CuO-SH outer layer (Fig. 1d), confirming the presence of DDT. The functionalized catalyst showed a notable shift in the absorption edge observed in X-ray absorption near-edge structure (XANES) spectra (Fig. 1e) compared to pristine CuO, from 8981.65 eV to 8979.73 eV in First derivative normalized absorption (inset in Fig. 1e)^{29,30}, indicating the DDT reduced Cu²⁺ species to form a surface of Cu¹⁺ (Fig. 1f). A new S2p peak was detected at 163 eV consistent with the Cu-S bonds (Fig. 1g)³¹. The successful functionalization with the DDT was further corroborated through attenuated total reflectance-Fourier transform infrared (ATR-FTIR) spectroscopy (Supplementary Fig. 4).

CO₂RR catalytic performance

To evaluate the CO₂RR activity of the DDT-modified hierarchical nanoelectrode, the electrocatalytic CO₂RR performance was measured in an H-type electrochemical cell with a CO₂-saturated 0.1 M KHCO₃ electrolyte at applied potentials from –0.8 to –1.6 V. The products were characterized by nuclear magnetic resonance (NMR) and gas chromatography (GC) (See details in the Methods section), including CO, formate, CH₄, and C₂₊ products (ethylene and ethanol). Figure 2a illustrates ethylene as the primary product of the CuO-SH catalyst, with ethylene selectivity gradually increasing with rising overpotential, reaching a peak Faraday efficiency (FE) of 72% at –1.4 V. In contrast, the unmodified CuO electrode shows a diverse distribution of products, comprising C₁ products (CO, formate) and H₂ (Fig. 2b). As the applied potential decreases, the FE of C₂₊ products for CuO diminishes, and the FE for H₂ rises to 58.9% at –1.6 V, where H₂ becomes the predominant product. However, the FE of H₂ for CuO-SH at the same potential is less than 10%, indicating a substantially suppressed HER. To visually represent the influence of DDT modification on the C₂₊ products, the data is re-plotted in Fig. 2c. At –1.6 V, the C₂₊ FE of the CuO-SH electrode is 79.6%, contrasting with 16.9% for the original CuO electrode, with ethylene comprising the majority of C₂₊ products, showcasing an enhancement of more than 4-fold. The C₂₊/C₁ ratio in the CO₂RR products was also calculated. The ratio of 7.8 for CuO-SH at –1.4 V indicates a preference for CO intermediates to dimerize, producing C₂₊ products rather than C₁ species. In comparison, the C₂₊/C₁ products ratio on CuO (0.82 at –1.4 V) is much lower than that on CuO-SH. Furthermore, the ratio of FE for C₂H₄ products to hydrogen (FE_{C₂H₄}/FE_{H₂}) (Supplementary Fig. 5) further verifies the boosted activity of the C–C coupling steps on CuO-SH electrodes.

To illustrate the potential of CO₂ electrolysis for large-scale ethylene production, we employed a gas-diffusion-electrode-based flow-cell system equipped with the CuO-SH catalyst. The FE for ethylene product formation on the CuO-SH electrode is further augmented, reaching a maximum FE of 79.5% at –1.2 V, accompanied by a total current density of 304 mA cm^{–2}. Notably, the ethylene partial current density achieved an impressive 242 mA cm^{–2}, surpassing the majority of previous reports (Fig. 2d and Supplementary Table 2). In contrast, the highest C₂H₄ FE and partial current density on the CuO catalyst were 44.8% and 169.3 mA cm^{–2} (Fig. 2e). Furthermore, a prolonged stability test of CuO-SH in a flow cell was conducted. The ethylene FE of CuO-SH initiated at 73.6% and remained consistently high at 49.7% after 40 h of testing under a constant current density of 200 mA cm^{–2}, demonstrating superior stability compared to CuO, which dropped to less than 10% over the same duration (Supplementary Fig. 6). Consequently, DDT treatment not only significantly

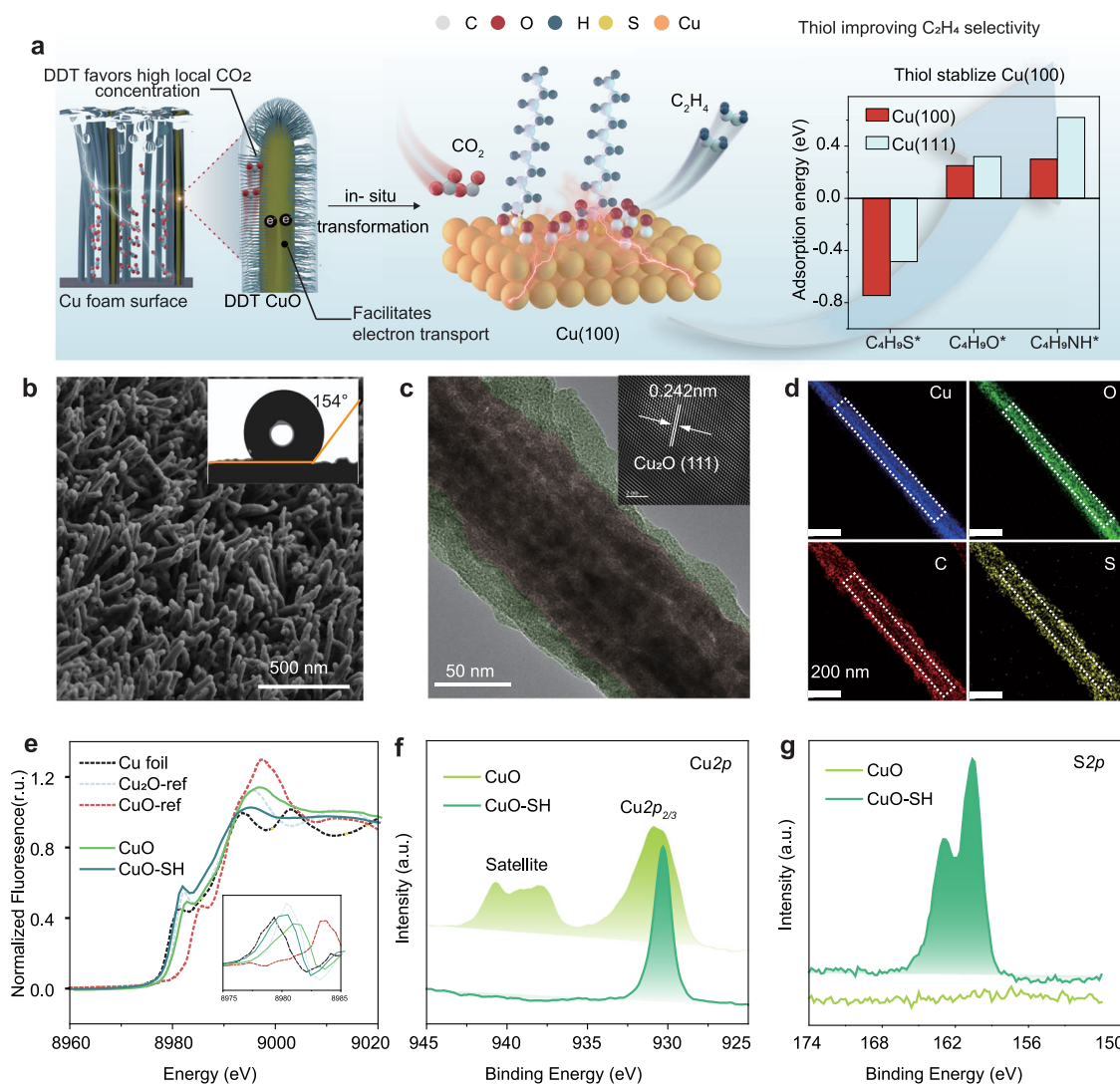


Fig. 1 | Schematic diagram of design and preparation process and characterizations of the DDT functionalized CuO-SH catalysts. **a** Schematic illustration for the design and preparation process of DDT modification strategy, and (Inset) DFT calculations of the adsorption energies of various alcohols, thiols, and amines with

alkyl chains. **b** Scanning electron microscope (SEM) image of CuO-SH electrode, (Inset) the contact angle measurements of CuO-SH. **c** TEM image, (Inset) FFT of HRTEM image and **(d)** EDS elemental mapping images of CuO-SH. **e** XANES spectra **(f)** Cu2p, **(g)** S2p XPS curves for CuO-SH and CuO.

enhances ethylene selectivity but also improves stability, showcasing its potential for practical applications in large-scale ethylene production through CO₂ electrolysis.

Despite the achieved increase in the FE of ethylene on CuO-SH through DDT modification, a gradual decrease in ethylene FE was observed during the stability test (Supplementary Figs. 6 and 7). Subsequently, an investigation was conducted to assess the stabilities of the thiol molecule on the CuO-SH electrode during the electrocatalytic process. The S2p, S K-edge XAFS and STEM-EDS mapping results confirm that the majority of DDT molecules remain during the CO₂RR (Supplementary Figs. 8 and 9). However, a new peak attributed to alkanesulfonates⁷ appeared at 168 eV in the S2p spectrum of CuO-SH after 5 h of reaction, becoming more pronounced with an extended reaction time of 40 h. Additionally, the S K-edge XAFS of the CuO-SH catalyst revealed an increase in the surface S valence state with prolonged reaction time at -1.4 V (Supplementary Fig. 8b). Further analysis of the S2p spectrum of CuO-SH revealed that, although most of the DDT remained intact, there was still a 17.3% DDT loss which was confirmed by the repetitive experiments (Supplementary Fig. 10). Consequently, we attribute the performance degradation of CuO-SH primarily to the partial loss of thiol groups, either through oxidation or

detachment (Supplementary Fig. 11). To further verify the impact of thiols on stability, thiols were used to retreat the CuO-SH samples after stability testing. The retreatment achieved a 27.5% increase in surface thiols recovery, leading to an improvement in the FE of ethylene (from 46.3 to 64.1%) (Supplementary Fig. 12). Following two rounds of retreatment, the ethylene FE consistently maintained a relatively high level (52.1%) after 160 h of operation, demonstrating the enhanced stability of the CuO-SH catalyst (Fig. 2f).

We infer that the improvement in C₂H₄ selectivity resulting from DDT modification can be attributed to three key contributions: enhanced CO₂ transport, increased coverages of *CO, and intrinsic activity. As mentioned earlier, DDT induces a hydrophobic surface on the electrode, leading to the formation of a three-phase interface. The ATR-FTIR spectrum indeed reveals that this hydrophobic interface enhances the local CO₂ concentration, indicating that DDT facilitates CO₂ transportation and inhibits the competing HER reaction. (Supplementary Figs. 13 and 14).

To clarify the effect of DDT on the *CO coverages during CO₂RR, we conducted a potential-dependent in situ Raman spectroscopy study in a CO₂-saturated 0.1M KHCO₃ electrolyte, enabling real-time monitoring surface adsorbates and quantification of adsorbed *CO

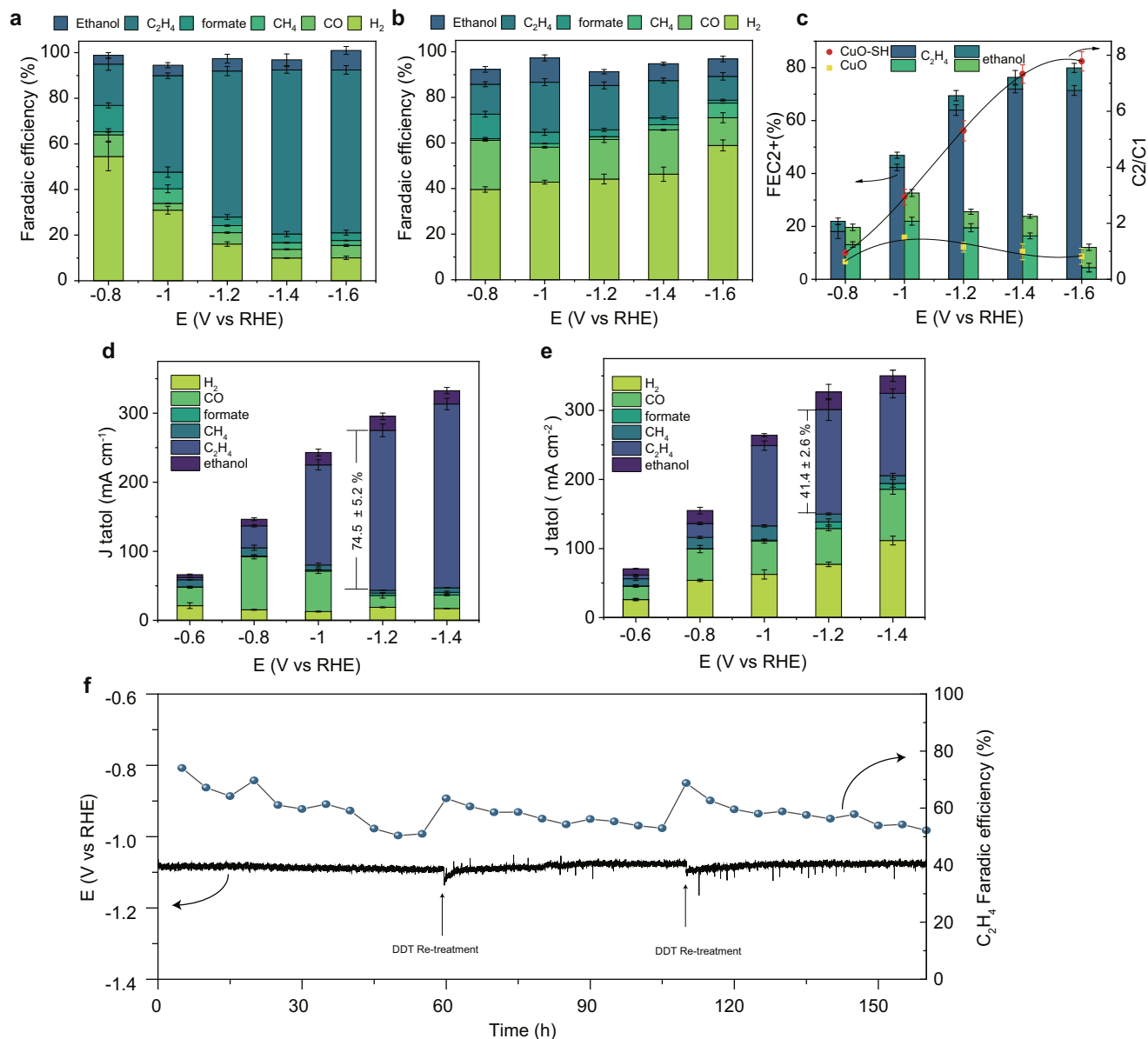


Fig. 2 | CO₂RR performances for the CuO and CuO-SH. Faradaic efficiencies (FE) of the CO₂RR products as a function of applied potential over (a) CuO-SH and (b) CuO, c FE values for C₂+ products and FE ratio of C₂+ products over C₁ products over CuO-SH and CuO at various potentials ranging from -0.8 to -1.6 V, current

densities and product distributions at different potentials over (d) CuO-SH and (e) CuO under flow cell measurement, f Stability test for CuO-SH at the current density 200 mA cm⁻² in a flow cell. The potential was corrected with 85% iR compensation. Error bars indicate the standard deviation of three independent measurements.

coverages at a range of applied potentials from the open-circuit potential (OCP) to -1.2 V on CuO-SH and CuO catalysts. Figure 3a, b illustrates that both electrodes exhibit two peaks at -1313 and -1616 cm⁻¹, attributed to the glassy carbon substrate³². An absorption band centered at -2057 cm⁻¹ starts to appear from a cathodic potential of -0.2 V for both CuO-SH and CuO catalysts, typically assigned to C=O stretching of the atop-adsorbed *CO species³³. The peak intensity of CO adsorption gradually increases when shifting to a more negative potential, indicating a higher *CO coverage derived from the activated CO₂. For a more accurate comparison of the CO peak intensities between the two samples, we normalize the CO characteristic peaks using the glassy carbon peaks as a reference (Supplementary Fig. 15). As depicted in Fig. 3c, the CuO-SH catalyst exhibits a higher CO peak intensity than CuO, signifying that DDT surface modification enhances CO adsorption strength. Simultaneously, it is observed that the *CO atop Raman peak shifted toward lower Raman shift (Fig. 3d). By comparing the peak positions of the CO adsorption peaks, we note

that within this potential range, the CO adsorption peak of CuO-SH is slightly lower than that of CuO, indicating a stronger CO binding ability of CuO-SH.

In addition to CO₂ transport and the adsorption of *CO intermediates, the C-C coupling is paramount for achieving high C₂H₄ selectivity. We further explored the impact of DDT modification on the intrinsic activity of the catalyst for the C-C coupling. To minimize the effect of the electrochemically active surface area (ECSA), we employed the double layer capacity (Cdl) method to measure the ECSA of the electrodes. The CuO-SH electrode exhibited an ECSA of 11.9 mF cm⁻², lower than that of unmodified CuO (16.4 mF cm⁻²) (Supplementary Fig. 17c). Subsequently, we normalized the partial current density of C₂H₄ products based on ECSA (Supplementary Fig. 17d). Despite the reduction in ECSA due to DDT modification, the CuO-SH delivers a superior ECSA-normalized C₂H₄ current density (2.93 mA mF⁻¹) compared to CuO (0.12 mA mF⁻¹) at -1.6 V, indicating that DDT significantly enhances the intrinsic activity of the C-C coupling.

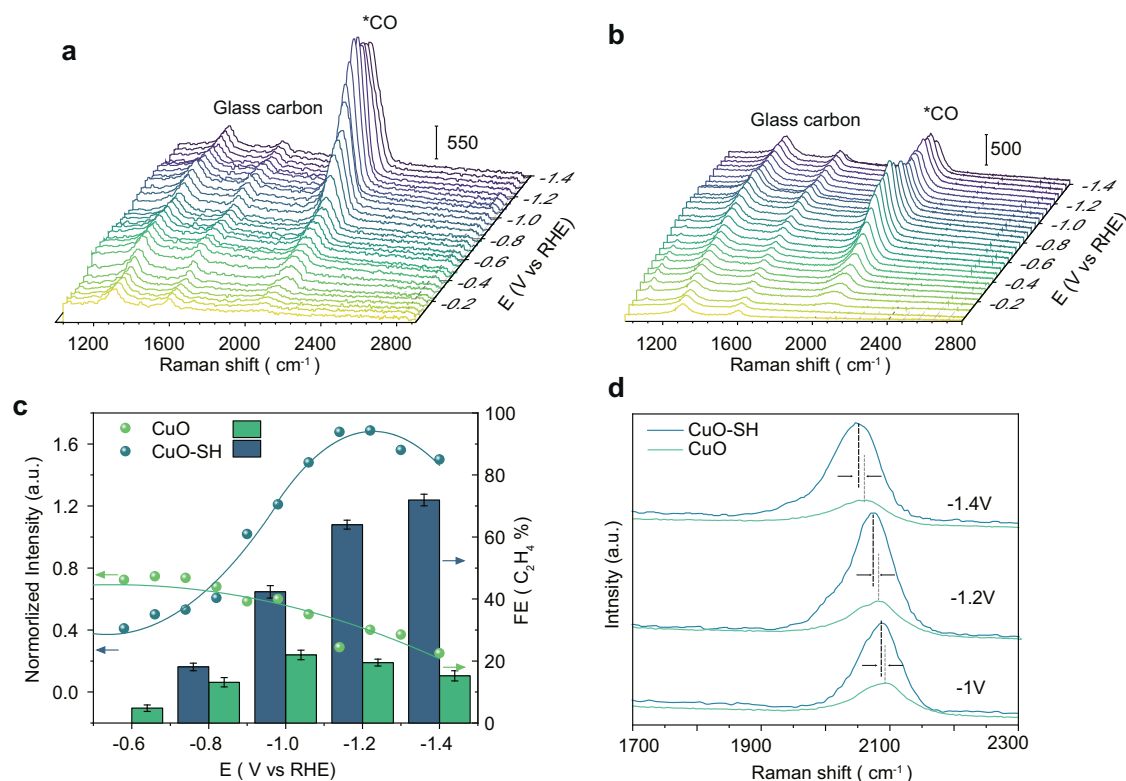


Fig. 3 | In situ Raman spectra. In situ Raman spectra of (a) CuO-SH and (b) CuO obtained in a potential window OCP to -1.4 V, c Potential dependence of the normalized intensity of *CO and FE of C_2H_4 (error bars indicate the standard deviation

of three independent measurements), d in situ Raman spectra of CuO-SH and CuO collected at different applied potential.

To gain deeper insights into the improved intrinsic activity of the C-C coupling, in situ XAS experiments were conducted to discern the evolution of the local structure of the catalysts. XANES spectra showcased a shift in absorption edge toward lower energies, indicating the reduction of cupric oxides during CO_2RR . Both the CuO-SH catalysts and the unmodified CuO samples underwent conversion to metallic Cu, as evidenced in Supplementary Fig. 18. Subsequently, we conducted fitting of the extended X-ray absorption fine structure (EXAFS) spectra at the Cu K -edge of both CuO-SH and CuO samples (Fig. 4a, b and Supplementary Figs. 19 and 20). The Cu–Cu coordination number in CuO-SH is around 9 at -1.6 V (Fig. 4c and Supplementary Table 3), which is lower than that of bulk face-centered cubic Cu and CuO, while that of the pristine CuO exceeded 10. This implies the formation of more unsaturated coordination structures in CuO-SH, serving as potential active sites.

We then conducted operando XRD experiments to scrutinize the structural transitions of CuO-SH and CuO catalysts during CO_2RR . As depicted in Fig. 4d, e, the characteristic peaks of copper oxide gradually diminished and disappeared at -0.8 V. In contrast, the intensity of XRD peaks corresponding to metallic Cu(111) and Cu(100) increased as the potential gradually shifted to -1.4 V, as confirmed by HRTEM imaging (Supplementary Fig. 21). According to surface energy calculations¹⁸, the Cu(111) facet with a surface energy of 1.25 J cm^{-2} is more stable than Cu(100) with a surface energy of 1.43 J cm^{-2} . Interestingly, the XRD results of Cu nanocatalysts derived from CuO-SH exhibited a higher intensity of the Cu(100) peaks compared to the CuO sample. Furthermore, we plotted the potential-dependent (100)/(111) crystal plane ratio and C_2H_4 selectivity trend to elucidate the contribution of crystal structure to ethylene selectivity (Fig. 4f). After normalization of XRD peak intensities, the Cu(100)/(111) intensities ratio of CuO-SH was over 3 times that of CuO at -1.4 V. Given that different copper facets display distinct OH^- electrochemical adsorption behavior, the OH^- electroadsorption experiment was conducted to

further analyze the surface structure of CuO and CuO-SH at the potentials ranging from -1 to -1.4 V. As shown in Supplementary Fig. 22, linear sweep voltammetry profiles revealed electrochemical OH^- adsorption peaks on Cu(100), Cu(110) and Cu(111) at potentials 0.36, 0.42, and 0.47 V versus RHE, respectively. In the OH^- adsorption analysis, we observed a high Cu(100)/Cu(111) ratio of 1.16, 1.04, and 1.09 at potentials ranging from -1 to -1.4 V vs. RHE, respectively, consistent with the results of the in situ XRD measurements. This trend indicates that DDT molecules stabilize Cu(100), leading to the preferential generation of Cu(100) surfaces during CO_2RR . Additionally, the in situ XRD of DDT-treated Cu(100) single crystal foil further confirms that DDT is beneficial for stabilizing Cu(100) during the CO_2RR reaction (Supplementary Fig. 23).

A positive correlation exists between the FE of ethylene and the (100)/(111) ratio of Cu derived from CuO and CuO-SH (Fig. 4f). To elucidate which crystal facet exhibits higher activity for ethylene selectivity, we employed well-defined Cu(100) and Cu(111) single crystal foil as a simplified model to eliminate the influence of other factors. The corresponding CO_2RR performances indicate that although the ethylene conversion efficiency of both single crystal foils is not high, Cu(100) unequivocally demonstrates a higher ethylene FE than Cu(111) (Supplementary Figs. 24 and 25). To understand the impact of catalyst facets on ethylene selectivity under real condition, we further investigated the time-dependent ethylene selectivity with the structural evolution of CuO-SH. We collected the time-resolved in situ XRD of CuO-SH at -1.4 V in 0.1 M $KHCO_3$ and also conducted the time-dependent performance testing over the CuO-SH electrode at -1.4 V (Supplementary Fig. 26). To observe the transformation process of crystal planes, it is worth noting that the CuO-SH samples used in this test were not subjected to activation treatment. As shown in Supplementary Fig. 26, the diffraction peak of Cu(100) gradually increases within the first 40 min, and the ratio of Cu(100)/Cu(111) stabilizes around 1 after 60 min. Correspondingly, the ethylene FE also

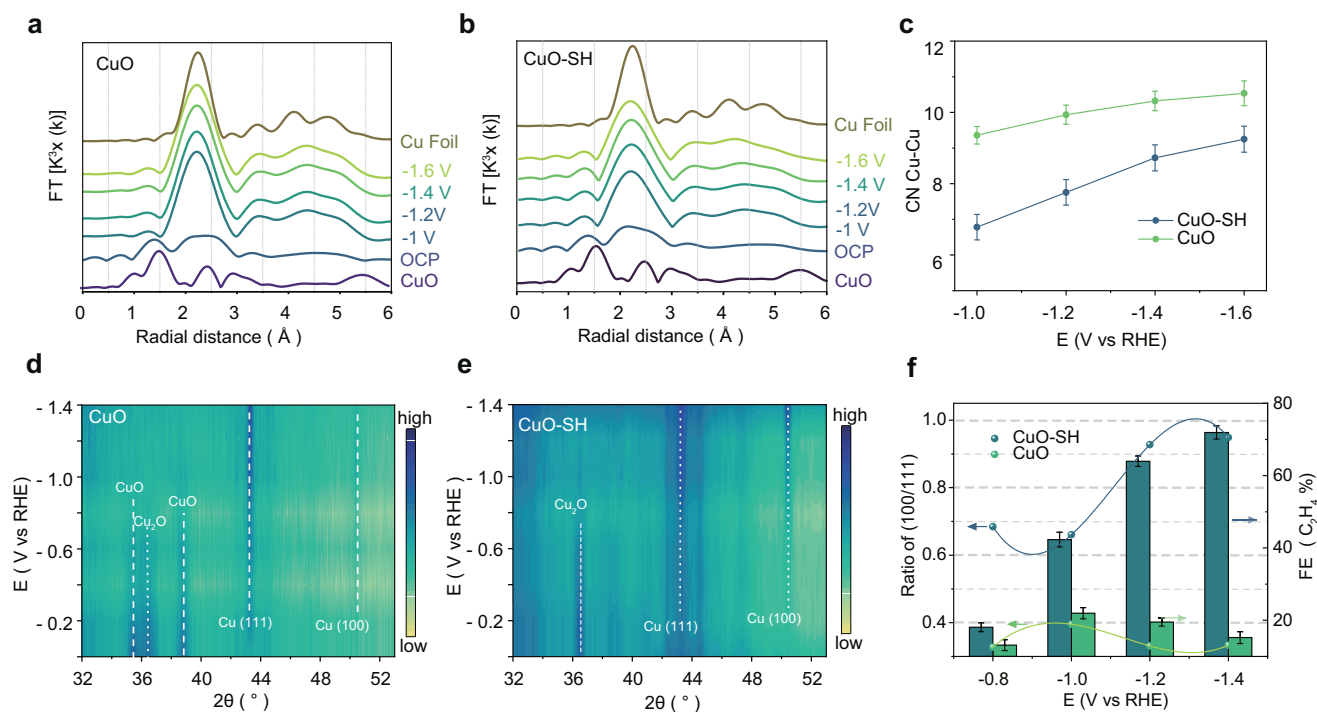


Fig. 4 | In situ XAFS and in situ XRD results. Fourier transform curves of in situ EXAFS at the Cu K-edge of the (a) CuO-SH and (b) CuO obtained in a potential window -1 to -1.6 V, c Coordination numbers of the first intermetallic Cu-Cu shell (error bars represent the fit error), In situ XRD patterns of (d) CuO-SH and (e) CuO

collected at various potentials ranging from 0 to -1.4 V, f Quantitative peak analysis: the ratio of Cu(100) and Cu(111) facets (error bars indicate the standard deviation of three independent measurements).

gradually increases with Cu(100) formation within the first 35 min and then reaches the maximum value. Whether using single crystal Cu foils or examining the time-dependent ethylene selectivity with structural evolution, it has been reaffirmed that Cu(100) possesses a higher ethylene FE than Cu(111), and the improved Cu(100) is responsible for the enhancement of ethylene selectivity in CuO-SH.

We probed the structural stability of the CuO-SH catalyst through the stability test. The time-dependent in situ XRD at -1.4 V showed that the CuO-SH catalyst then maintains a relatively stable crystal structure after being reduced (Supplementary Fig. 26b). Additionally, the XRD results of CuO-SH after the 40 h stability test indicated a slight reduction in the Cu(100) facets of the catalyst, as evidenced by a decrease in the Cu(100)/Cu(111) ratio from 1.09 at 2 h to 0.87 at 40 h (Supplementary Fig. 27). The reduction of Cu(100) facets may be attributed to the partial conversion of DDT, thus leading to a decrease in the ethylene FE of the CuO-SH in the stability tests.

Mechanistic studies

As proposed in prior literature, the generation of multi-carbon products during CO₂RR could occur through the dimerization of two *CO intermediates^{24,34} or *CO-COH intermediates³⁵⁻³⁷. Therefore, the ATR-FTIR was performed to elucidate the C-C coupling mechanism on CuO-SH during CO₂RR. The IR spectra were collected from the OCP to -1.4 V after the pre-reduction of both the CuO and CuO-SH catalysts. The peaks at -2043 cm⁻¹ and -1890 cm⁻¹ correspond to the atop-adsorbed *CO (CO_L) and bridge-bond CO (CO_B) intermediates, respectively, which are widely used as indicators of the CO coverage over the catalysts surfaces^{34,38-40}. Moreover, a marked tuning of *CO_L is observed as the potential becomes more negative (Supplementary Fig. 29 and Supplementary Table 4). The CuO-SH catalysts show a stronger infrared band for *CO_L compared to the unmodified CuO (Fig. 5a, b and Supplementary Fig. 30). The peak position of CO adsorbed on CuO-SH closely overlapped with that on Cu(100) foil, while the CO peak position of CuO is closer to Cu(111) foil. Based on the

in situ IR spectra through an internal standard, the Cu(100) foil showed a greater normalized CO intensity, indicating stronger CO adsorption compared to the Cu(111) foil, in agreement with our DFT results (Supplementary Figs. 31-33). The improved coverage of *CO_L could be attributed to the increased proportion of Cu(100) facets on the CuO-SH surface. These variations in CO adsorption behavior indicate that the DDT treatment improves the binding strength of *CO on CuO-SH, leading to enhanced *CO coverage, in agreement with the Raman experiments. Notably, the *CHO species adsorbed on CuO-SH are observed in Fig. 5a, with peak⁴¹ located at -1720 cm⁻¹, representing a crucial intermediate for C-C asymmetric coupling.

Our DFT results indicated that the *CHO intermediate on CuO-SH derived from *CO_L has a lower protonation energy barrier on Cu(100) than *CO_B (Supplementary Fig. 34). Furthermore, the additional peak at -1586 cm⁻¹ and -1236 cm⁻¹ collected on the CuO-SH catalyst are indexed to the adsorbed *CO-CHO intermediates (Fig. 5a)⁴². Therefore, the C-C coupling on CuO-SH could be asymmetrically triggered between *CO and *CHO. The ATR-FTIR results provide experimental evidence of the asymmetric coupling process.

Finally, we performed DFT calculations to gain a deeper understanding the mechanism underlying the significantly enhanced activity and selectivity toward the ethylene due to DDT modification. To truncate the carbon chain length of thiol used for DFT calculations, the adsorption energies of thiols with varied carbon chain lengths were calculated. *C₄H₉S was selected because the adsorption energy converges on the number of carbon atoms reaching four (Supplementary Fig. 35). *CO-*CHO was experimentally characterized as the prominently intermediate adsorbate on thiol-modified copper surfaces (Fig. 5a), indicating the necessity of investigating the activation energy barrier of CO-CHO coupling. Due to the sluggish kinetics and the high thermodynamic energy barrier of the C-C coupling step, it is commonly considered the rate-limiting step for CO₂RR⁴³. The activation free energy barriers of CO-CHO coupling were calculated on four representative surfaces of Cu(100), Cu(100) with *C₄H₉S, Cu(111) and

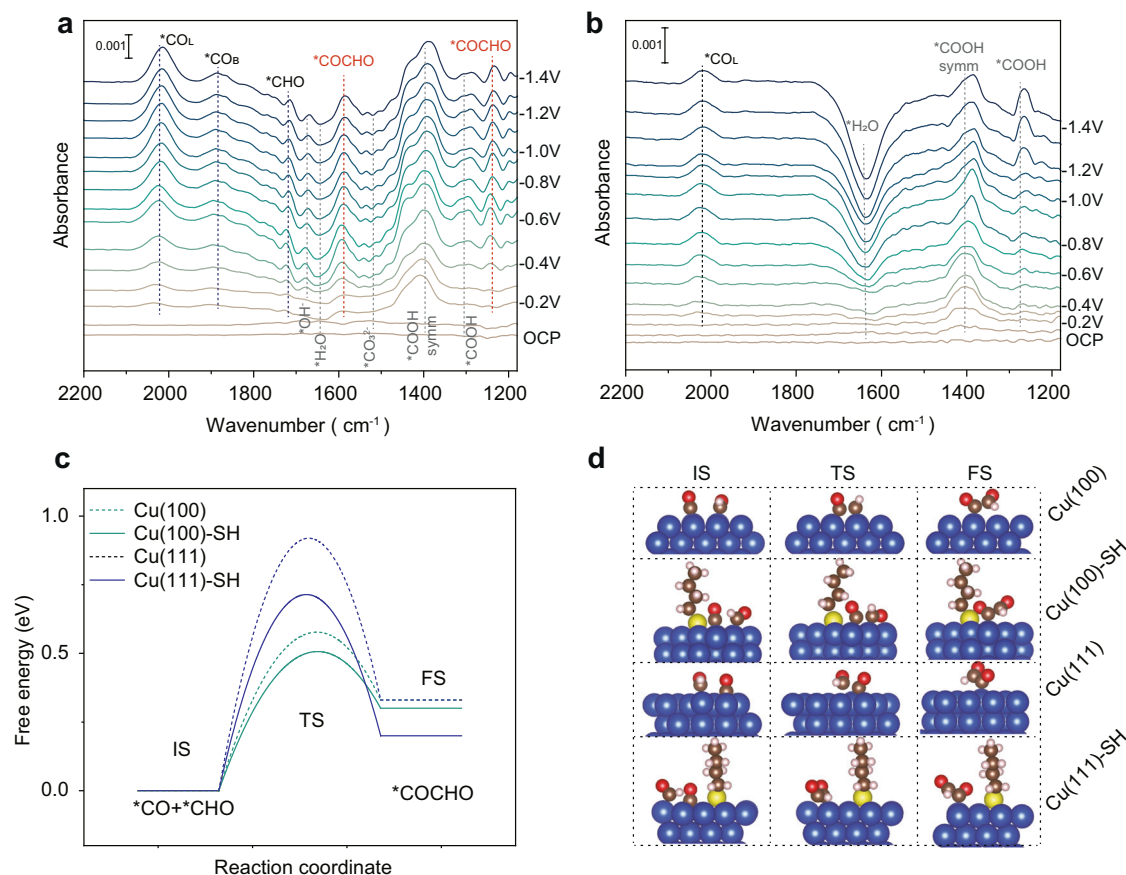


Fig. 5 | Mechanistic studies. In situ ATR-FTIR recorded at different applied potentials for (a) CuO-SH and (b) CuO catalysts. The free energy diagram (c) and optimized structures (d) of the CO-CHO coupling process on the Cu(100), Cu(100)

with *C_4H_9S , Cu(111) and Cu(111) with *C_4H_9S surfaces. Blue sphere: Cu, yellow sphere: S, brown sphere: C, pink sphere: H, red sphere: O.

Cu(111) with *C_4H_9S (Fig. 5c and Supplementary Table 5). The initial state (*CO co-adsorbed with *CHO) and final state (*COCHO) structures of CO-CHO coupling were determined based on our previous work⁴⁴ that has already taken into account the different adsorption sites and the steric hindrance of relative positions of *CO and *CHO , as well as *COCHO (Fig. 5d). We found that the activation barrier of CO-CHO coupling on Cu(100) is 0.35 eV lower than that on Cu(111). The modification of *C_4H_9S on Cu(100) can further reduce the barrier by about 0.07 eV, leading to the improved activity and selectivity of C_{2+} products, consistent with experimental observations (Fig. 2c). Moreover, the analysis of charge density difference between initial state and final state shows that thiol stabilizes the intermediate product *COCHO (Supplementary Fig. 36), consistent with the reduced free energy changes of CO-CHO coupling step on Cu surfaces with adsorbed *C_4H_9S (Fig. 5a).

In summary, we employed a hierarchical nanostructured CuO electrode functionalized with DDT to achieve superior selectivity of CO_2RR for ethylene. By DDT treatment, the electrode exhibited a significant enhancement in FE of C_2H_4 products, reaching 72%, which is more than four times higher than the untreated electrode. Our in situ experiments results show that the DDT treatment facilitates CO_2 transport, enhances CO coverage on the catalyst surfaces, and stabilizes Cu(100), thus promoting the C-C coupling. Theoretical calculations further confirmed that the DDT-stabilized Cu(100) surface can effectively reduce the activation energy barrier of C-C coupling between *CO and *CHO . A techno-economic analysis demonstrated promising potential for future applications (Supplementary Table 7). Our findings provide valuable insights into the mechanism of CO_2RR to ethylene and offer an opportunity to develop more efficient Cu-based

electrocatalysts for the highly selective conversion of CO_2 to high-value-added chemicals and fuels.

Methods

Preparation of electrode

$Cu(OH)_2$ was grown on a piece of Cu foam (1 cm \times 3 cm) through anodization following a protocol that involved washing the foam with HCl, ultrasonic cleaning in acetone, ethanol, and deionized water, and anodization at 20 mA cm^{-2} for 20 min in 1 M NaOH. Annealing at 250 $^{\circ}C$ for 1 h converted $Cu(OH)_2$ nanowires to black CuO. Surface modification was achieved by submerging the CuO/Cu foam electrode in 1-dodecanethiol for 20 min at room temperature, followed by ethanol washing to remove excess 1-dodecanethiol and drying in ambient conditions by purging with compressed N_2 .

Materials characterization

The surface composition and valence states were analyzed with XPS, using an Escalab 250Xi X-ray photoelectron spectrometer (Thermo Fisher) with Al K α (1486.6 eV) X-rays as the excitation source, and the binding energy of the C 1s peak at 284.8 eV was taken as an internal reference. The morphologies were examined by SEM conducted on a Hitachi SU4800 scanning electron microanalyzer with an accelerating voltage of 15 kV. Powder X-ray diffraction (PXRD) patterns were taken on PANalytical X-pert diffractometer (PANalytical, Netherlands) with Cu K α radiation at 40 kV and 40 mA at room temperature. Transmission electron microscope (TEM) images were conducted on FEI Talos F200X G2 TEM equipment. HAADF-STEM images and energy dispersive spectra (EDS) elemental mapping were conducted on FEI Themis Z TEM equipment.

Electrochemical measurements

Electrochemical measurements were performed using a two-compartment cell separated by a Nafion membrane (N-115, DuPont) and controlled by an electrochemical workstation (CHI660E). Each compartment contained 40 ml of 0.1 M KHCO₃ (Supplementary Fig. 37), with a Pt mesh (1 cm × 1 cm × 0.2 cm) and a calibrated Ag/AgCl electrode serving as the counter and reference electrodes, respectively. The working electrode area was 1 cm² (0.5 cm × 1 cm × 2 side). Prior to electrochemical measurements, CO₂ was continuously purged into the cathodic compartment for at least 30 min. During measurements, CO₂ was bubbled into the electrolyte with a constant flow rate of 20 sccm controlled by a digital mass flow controller. For the flow-cell experiment, a 1 cm² gas-diffusion electrode coated with 400 μl of well-mixed catalyst ink containing 20 μl of Nafion dispersion and cathode electrocatalyst was used as the cathode, giving a catalyst loading of 1 mg cm⁻², with Ni foam serving as the anode and Hg/HgO. The cathode catalyst is obtained by mechanical and ultrasonic exfoliation of the catalyst from the CuO or CuO-SH electrode. Two parallel fluxes of 1 M KOH were injected into the cathodic and anodic channels separated by an anion-exchange membrane. The CO₂ flow rate was 30 sccm, controlled by a mass flow controller. The resistance of 11.2 ± 0.1 Ω (H-cell) and 3.4 ± 0.2 Ω (flow cell) was used to calculate the iR-correction (Supplementary Fig. 39).

All potentials were calibrated to the RHE scale using the equation:

$$E(\text{RHE}) = E_{\text{applied}} + 0.059 \times \text{pH} + E_{\text{reference}}(V)(E_{\text{Ag/AgCl}}) \\ = 0.197V, E_{\text{Hg/HgO}} = 0.098V \quad (1)$$

Gas products were quantitatively analyzed using gas chromatography equipped with flame ionization and thermal conductivity detectors (Hui fen 9890E). Liquid products were collected after at least 0.5 h of electrolysis and quantitatively analyzed using 1H NMR spectroscopy with H₂O suppression. The internal standard consisted of 400 μl electrolyte mixed with 50 μl dimethyl sulfoxide (20 mM) and 100 μl D₂O.

The FE value of a specific product was calculated based on the following equation:

$$FE_{\text{gas}} = \frac{Q_{\text{gas}}}{Q_{\text{total}}} = \frac{n_{\text{gas}}NF}{Q_{\text{total}}} = \frac{(\frac{\nu}{60S/\text{min}}) \times (\frac{y}{22,400\text{cm}^3/\text{mol}})NF}{j} \times 100\% \quad (2)$$

$$FE_{\text{liquid}} = \frac{Q_{\text{liquid}}}{Q_{\text{total}}} = \frac{n_{\text{liquid}}NF}{Q_{\text{total}}} = \frac{n_{\text{liquid}}NF}{j \times t} \times 100\% \quad (3)$$

where ν is the gas flow rate measured by a flowmeter, y is the volume concentration of gas products, N represents the number of transferred electrons for each product, F denotes the Faraday constant (96,500 C mol⁻¹), j signifies current, t corresponds to the running time, and n_{liquid} (in moles) represents the amount of liquid products determined 1H NMR.

In situ XAFS measurements

The in situ XAS measurements were carried out using a custom-made electrochemical cell with a flat wall and a circular orifice of 15 mm diameter⁴⁵ (Supplementary Fig. 40). The catalyst-modified carbon paper was employed as the working electrode in aqueous electrolyte of 0.1 M KHCO₃ saturated by CO₂. The reference and counter electrodes were a Pt plate, and Ag/AgCl (saturated with KCl), respectively. These in situ XAS investigations were performed at the 1W2B beamline of the Beijing Synchrotron Radiation Facility (BSRF) in fluorescence mode, with the applied potential controlled by a CHI 660E electrochemical workstation. A Cu metal foil was used for calibration of the X-ray energy.

In situ ATR-FTIR

The in situ ATR-FTIR investigations were carried out with the Bruker INVENIO spectrometer with a HgCdTe (MCT) detector cooled with liquid nitrogen. A customized electrochemical H-cell was used to collect the in situ ATR-FTIR spectra, in which Pt-wire and Ag/AgCl served as counter and reference electrodes, respectively. A fixed-angle Si prism (60°) coated with catalysts was used as the working electrode (Supplementary Fig. 41). 0.1 M KHCO₃ aqueous solution constantly purged with CO₂ was employed as the electrolyte. All spectra were collected with 128 scans and a resolution of 4 cm⁻¹.

In situ Raman and XRD

In situ Raman measurements were carried out by utilizing a Spectro-electrochemical flow cell. Raman measurements were conducted using a Micro-Raman spectrometer (ActonSP2500, PI) and a ×50 objective (Leica) equipped with a 785 nm laser. An Ag/AgCl electrode and a Pt plate were used as the reference and counter electrodes respectively (Supplementary Fig. 42). In situ XRD was performed at Rigaku Smart lab, and CO₂ electrolysis was conducted using a three-electrode electrochemical cell, with the Ag/AgCl electrode and Pt wire as the reference electrode and counter electrode, respectively (Supplementary Fig. 43). To prepare the working electrode, the catalyst ink was dropped onto a hydrophobic carbon paper. Data was collected in the electrode potential region from 0 to -1.6 V versus RHE. In situ XRD signals were collected from 30° to 60° with a scan rate of 20° min⁻¹.

Computational methods

All the periodic DFT calculations were performed by the Vienna ab initio simulation package (VASP)^{46,47}. The electron exchange correlation energy was described using a function of the revised Perdew-Burke-Ernzerhof (RPBE)⁴⁸ at Generalized Gradient Approximation (GGA) level⁴⁹. Spin polarization was considered in the calculations, and the Methfessel-Paxton method⁵⁰ of order 2 with a smearing parameter of 0.2 eV was employed to determine the electron occupancies. Real-space projectors were used to evaluate the non-local part of the PAW potential. Additional details of the DFT calculations are provided in the Supporting Information.

Data availability

Additional data related to this study are available from the corresponding author upon request.

References

- Langie, K. M. G. et al. Toward economical application of carbon capture and utilization technology with near-zero carbon emission. *Nat. Commun.* **13**, 7482 (2022).
- Chen, X. Y. et al. Electrochemical CO₂-to-ethylene conversion on polyamine-incorporated Cu electrodes. *Nat. Catal.* **4**, 20–27 (2021).
- Wei, P. et al. Coverage-driven selectivity switch from ethylene to acetate in high-rate CO₂/CO electrolysis. *Nat. Nanotechnol.* **18**, 299–306 (2023).
- Li, W. Z. et al. Bifunctional ionomers for efficient co-electrolysis of CO₂ and pure water towards ethylene production at industrial-scale current densities. *Nat. Energy* **7**, 835–843 (2022).
- Lim, C. Y. J. et al. Surface charge as activity descriptors for electrochemical CO₂ reduction to multi-carbon products on organic-functionalised Cu. *Nat. Commun.* **14**, 335 (2023).
- Zhang, W. et al. Atypical oxygen-bearing copper boosts ethylene selectivity toward electrocatalytic CO₂. *Reduct. J. Am. Chem. Soc.* **142**, 11417–11427 (2020).
- Zhou, Y. S. et al. Dopant-induced electron localization drives CO₂ reduction to C₂ hydrocarbons. *Nat. Chem.* **10**, 974–980 (2018).
- Hori, Y., Kikuchi, K. & Suzuki, S. Production of CO and CH₄ in electrochemical reduction of CO₂ at metal-electrodes in aqueous hydrogencarbonate solution. *Chem. Lett.* **14**, 1695–1698 (1985).

9. Birdja, Y. Y. et al. Advances and challenges in understanding the electrocatalytic conversion of carbon dioxide to fuels. *Nat. Energy* **4**, 732–745 (2019).
10. Nitopi, S. et al. Progress and perspectives of electrochemical CO₂ reduction on copper in aqueous electrolyte. *Chem. Rev.* **119**, 7610–7672 (2019).
11. Gao, D., Aran-Ais, R. M., Jeon, H. S. & Roldan Cuenya, B. Rational catalyst and electrolyte design for CO₂ electroreduction towards multicarbon products. *Nat. Catal.* **2**, 198–210 (2019).
12. De Arquer, F. P. G. et al. CO₂ electrolysis to multicarbon products at activities greater than 1 A cm⁻². *Science* **367**, 661 (2020).
13. Chen, C. et al. Exploration of the bio-analogous asymmetric C-C coupling mechanism in tandem CO₂ electroreduction. *Nat. Catal.* **5**, 878–887 (2022).
14. Ross, M. B. et al. Designing materials for electrochemical carbon dioxide recycling. *Nat. Catal.* **2**, 648–658 (2019).
15. Montoya, J. H., Shi, C., Chan, K. & Norskov, J. K. Theoretical insights into a CO dimerization mechanism in CO₂ electroreduction. *J. Phys. Chem. Lett.* **6**, 2032–2037 (2015).
16. Moller, T. et al. Electrocatalytic CO₂ reduction on CuO_x nanocubes: tracking the evolution of chemical state, geometric structure, and catalytic selectivity using operando spectroscopy. *Angew. Chem. Int. Ed.* **59**, 17974–17983 (2020).
17. Louidice, A. et al. Tailoring copper nanocrystals towards C₂ products in electrochemical CO₂ reduction. *Angew. Chem. Int. Ed.* **55**, 5789–5792 (2016).
18. Wang, Y. H. et al. Catalyst synthesis under CO₂ electroreduction favours faceting and promotes renewable fuels electrosynthesis. *Nat. Catal.* **3**, 98–106 (2020).
19. Aran-Ais, R. M. et al. The role of in situ generated morphological motifs and Cu(i) species in C₂₊ product selectivity during CO₂ pulsed electroreduction. *Nat. Energy* **5**, 317–325 (2020).
20. Wang, J. L. et al. Linking the dynamic chemical state of catalysts with the product profile of electrocatalytic CO₂ reduction. *Angew. Chem. Int. Ed.* **60**, 17254–17267 (2021).
21. Wu, H. L. et al. Improved electrochemical conversion of CO₂ to multicarbon products by using molecular doping. *Nat. Commun.* **12**, 7210 (2021).
22. Simon, G. H., Kley, C. S. & Roldan Cuenya, B. Potential-dependent morphology of copper catalysts during CO₂ electroreduction revealed by in situ atomic force microscopy. *Angew. Chem. Int. Ed.* **60**, 2561–2568 (2021).
23. Zhong, D. Z. et al. Coupling of Cu(100) and (110) facets promotes carbon dioxide conversion to hydrocarbons and alcohols. *Angew. Chem. Int. Ed.* **60**, 4879–4885 (2021).
24. Hanselman, S., Koper, M. T. M. & Calle-Vallejo, F. computational comparison of late transition metal (100) surfaces for the electrocatalytic reduction of CO to C₂ species. *ACS Energy Lett.* **3**, 1062–1067 (2018).
25. Calle-Vallejo, F. & Koper, M. T. M. Theoretical considerations on the electroreduction of CO to C₂ species on Cu(100) electrodes. *Angew. Chem. Int. Ed.* **52**, 7282–7285 (2013).
26. De Gregorio, G. L. et al. Facet-dependent selectivity of Cu catalysts in electrochemical CO₂ reduction at commercially viable current densities. *ACS Catal.* **10**, 4854–4862 (2020).
27. Yu, S., Louisia, S. & Yang, P. The interactive dynamics of nanocatalyst structure and microenvironment during electrochemical CO₂ conversion. *JACS Au* **2**, 562–572 (2022).
28. Kohn, W. & Sham, L. J. Self-consistent equations including exchange and correlation effects. *Phys. Rev.* **140**, 1133 (1965).
29. De Luna, P. et al. Catalyst electro-redeposition controls morphology and oxidation state for selective carbon dioxide reduction. *Nat. Catal.* **1**, 103–110 (2018).
30. Wang, X. L. et al. Morphology and mechanism of highly selective Cu(II) oxide nanosheet catalysts for carbon dioxide electroreduction. *Nat. Commun.* **12**, 794 (2021).
31. Dilimon, V. S., Denayer, J., Delhalle, J. & Mekhalif, Z. Electrochemical and spectroscopic study of the self-assembling mechanism of normal and chelating alkanethiols on copper. *Langmuir* **28**, 6857–6865 (2012).
32. Zhan, C. et al. Revealing the CO coverage-driven C-C coupling mechanism for electrochemical CO₂ reduction on Cu₂O nanocubes via operando raman spectroscopy. *ACS Catal.* **11**, 7694–7701 (2021).
33. Gunathunge, C. M. et al. Spectroscopic observation of reversible surface reconstruction of copper electrodes under CO₂ reduction. *J. Phys. Chem. C* **121**, 12337–12344 (2017).
34. Kim, Y. et al. Time-resolved observation of C-C coupling intermediates on Cu electrodes for selective electrochemical CO₂ reduction. *Energy Environ. Sci.* **13**, 4301–4311 (2020).
35. Garza, A. J., Bell, A. T. & Head-Gordon, M. Mechanism of CO₂ reduction at copper surfaces: pathways to C₂ products. *ACS Catal.* **8**, 1490–1499 (2018).
36. Xiao, H., Cheng, T. & Goddard, W. A. Atomistic mechanisms underlying selectivities in C₁ and C₂ products from electrochemical reduction of CO on Cu(111). *J. Am. Chem. Soc.* **139**, 130–136 (2017).
37. Xiao, H., Cheng, T., Goddard, W. A. & Sundararaman, R. Mechanistic explanation of the pH dependence and onset potentials for hydrocarbon products from electrochemical reduction of CO on Cu (111). *J. Am. Chem. Soc.* **138**, 483–486 (2016).
38. Zhu, S. Q., Li, T. H., Cai, W. B. & Shao, M. H. CO₂ electrochemical reduction as probed through infrared spectroscopy. *ACS Energy Lett.* **4**, 682–689 (2019).
39. Katayama, Y. et al. An in situ surface-enhanced infrared absorption spectroscopy study of electrochemical CO₂ reduction: selectivity dependence on surface c-bound and o-bound reaction intermediates. *J. Phys. Chem. C* **123**, 5951–5963 (2019).
40. Chou, T. C. et al. Controlling the oxidation state of the Cu electrode and reaction intermediates for electrochemical CO₂ reduction to ethylene. *J. Am. Chem. Soc.* **142**, 2857–2867 (2020).
41. Zhu, S., Jiang, B., Cai, W.-B. & Shao, M. Direct observation on reaction intermediates and the role of bicarbonate anions in CO₂ electrochemical reduction reaction on Cu surfaces. *J. Am. Chem. Soc.* **139**, 15664–15667 (2017).
42. Qiu, X. F. et al. Highly selective CO₂ electroreduction to C₂H₄ using a metal-organic framework with dual active sites. *J. Am. Chem. Soc.* **143**, 7242–7246 (2021).
43. Zhuang, T. T. et al. Steering post-C-C coupling selectivity enables high efficiency electroreduction of carbon dioxide to multi-carbon alcohols. *Nat. Catal.* **1**, 421–428 (2018).
44. Raciti, D. et al. Low-overpotential electroreduction of carbon monoxide using copper nanowires. *ACS Catal.* **7**, 4467–4472 (2017).
45. Su, X. et al. Complementary operando spectroscopy identification of in-situ generated metastable charge-asymmetry Cu₂-CuN₃ clusters for CO₂ reduction to ethanol. *Nat. Commun.* **13**, 1322 (2022).
46. Kresse, G. & Furthmuller, J. Efficient iterative schemes for ab initio total-energy calculations using a plane-wave basis set. *Phys. Rev. B* **54**, 11169–11186 (1996).
47. Kresse, G. & Furthmuller, J. Efficiency of ab-initio total energy calculations for metals and semiconductors using a plane-wave basis set. *Comp. Mater. Sci.* **6**, 15–50 (1996).
48. Hammer, B., Hansen, L. B. & Norskov, J. K. Improved adsorption energetics within density-functional theory using revised Perdew-Burke-Ernzerhof functionals. *Phys. Rev. B* **59**, 7413–7421 (1999).
49. Perdew, J. P., Burke, K. & Ernzerhof, M. Generalized gradient approximation made simple. *Phys. Rev. Lett.* **77**, 3865–3868 (1996).
50. Methfessel, M. & Paxton, A. T. High-precision sampling for brillouin-zone integration in metals. *Phys. Rev. B.* **40**, 3616–3621 (1989).

51. Momma, K. & Izumi, F. VESTA: a three-dimensional visualization system for electronic and structural analysis. *J. Appl. Crystallogr.* **41**, 653–658 (2008).

Acknowledgements

The project was funded by China Petroleum and Chemical Corporation under grant No. 421058. L.C. acknowledges support from the National Natural Science Foundation of China under grant No. 22203072 and the Fundamental Research Funds for the Central Universities under award 226-2022-00167. Computational resources were provided by AI + High Performance Computing Center of Institute of Computing Innovation, Zhejiang University (ZJU-ICI). Atomic-scale structural images were generated using VESTA⁵¹.

Author contributions

Z.C. conceived and supervised the project. Y.C.Y. performed the experiments and conducted the data analysis with contributions from J.H.W., Y.Y.F., Y.C.L., W.X.C. and Z.C. Y.C.Y. and W.X.C. performed the XAS characterizations and conducted the XAS data analysis. L.C. and T.S. designed and performed the DFT calculations. Y.C.Y. and T.S. wrote the manuscript under guidance of L.C. and Z.C. All authors discussed the results and commented on the manuscript.

Competing interests

The authors declare no competing interests.

Additional information

Supplementary information The online version contains supplementary material available at <https://doi.org/10.1038/s41467-024-45704-2>.

Correspondence and requests for materials should be addressed to Liang Cao or Zhuo Chen.

Peer review information *Nature Communications* thanks the anonymous reviewers for their contribution to the peer review of this work. A peer review file is available.

Reprints and permissions information is available at <http://www.nature.com/reprints>

Publisher's note Springer Nature remains neutral with regard to jurisdictional claims in published maps and institutional affiliations.

Open Access This article is licensed under a Creative Commons Attribution 4.0 International License, which permits use, sharing, adaptation, distribution and reproduction in any medium or format, as long as you give appropriate credit to the original author(s) and the source, provide a link to the Creative Commons license, and indicate if changes were made. The images or other third party material in this article are included in the article's Creative Commons license, unless indicated otherwise in a credit line to the material. If material is not included in the article's Creative Commons license and your intended use is not permitted by statutory regulation or exceeds the permitted use, you will need to obtain permission directly from the copyright holder. To view a copy of this license, visit <http://creativecommons.org/licenses/by/4.0/>.

© The Author(s) 2024